Mechie, J., Abu-Ayyash, K., Ben-Avraham, Z., El-Kelani, R., Mohsen, A., Rümpker, G., Saul, J., Weber, M. (2005): Crustal shear velocity structure across the Dead Sea Transform from two-dimensional modelling of DESERT project explosion seismic data. - Geophysical Journal International, 160, 3, pp. 910—924.

DOI: http://doi.org/10.1111/j.1365-246X.2005.02526.x

Geophys. J. Int. (2005) **160,** 910–924 doi: 10.1111/j.1365-246X.2005.02526.x

Crustal shear velocity structure across the Dead Sea Transform from two-dimensional modelling of DESERT project explosion seismic data

J. Mechie,[1] K. Abu-Ayyash,[2] Z. Ben-Avraham,[3] R. El-Kelani,[4] A. Mohsen,[1] G. Rümpker,[1] J. Saul[1] and M. Weber[1,5]

[1] *GeoForschungsZentrum Potsdam (GFZ), Department* 2, *Telegrafenberg,* 14473 *Potsdam, Germany. E-mail: jimmy@gfz-potsdam.de*
[2] *Natural Resources Authority, Amman, Jordan*
[3] *Tel-Aviv University, Israel*
[4] *An-Najah National University, Nablus, Palestine*
[5] *Institut für Geowissenschaften, Universität Potsdam, Germany*

Accepted 2004 November 15. Received 2004 November 10; in original form 2004 April 9

SUMMARY

An analysis of the shear (*S*) waves recorded during the wide-angle reflection/refraction (WRR) experiment as part of the DESERT project crossing the Dead Sea Transform (DST) reveals average crustal *S*-wave velocities of 3.3–3.5 km s^{-1} beneath the WRR profile. Together with average crustal *P*-wave velocities of 5.8–6.1 km s^{-1} from an already published study this provides average crustal Poisson's ratios of 0.26–0.27 ($V_p/V_s = 1.76$–1.78) below the profile. The top two layers consisting predominantly of sedimentary rocks have *S*-wave velocities of 1.8–2.7 km s^{-1} and Poisson's ratios of 0.25–0.31 ($V_p/V_s = 1.73$–1.91). Beneath these two layers the seismic basement has average *S*-wave velocities of around 3.6 km s^{-1} east of the DST and about 3.7 km s^{-1} west of the DST and Poisson's ratios of 0.24–0.25 ($V_p/V_s = 1.71$–1.73). The lower crust has an average *S*-wave velocity of about 3.75 km s^{-1} and an average Poisson's ratio of around 0.27 ($V_p/V_s = 1.78$). No *Sn* phase refracted through the uppermost mantle was observed. The results provide for the first time information from controlled source data on the crustal *S*-wave velocity structure for the region west of the DST in Israel and Palestine and agree with earlier results for the region east of the DST in the Jordanian highlands. A shear wave splitting study using *SKS* waves has found evidence for crustal anisotropy beneath the WRR profile while a receiver function study has found evidence for a lower crustal, high *S*-wave velocity layer east of the DST below the profile. Although no evidence was found in the *S*-wave data for either feature, the *S*-wave data are not incompatible with crustal anisotropy being present as the WRR profile only lies 30° off the proposed symmetry axis of the anisotropy where the difference in the two *S*-wave velocities is still very small. In the case of the lower crustal, high *S*-wave velocity layer, if the velocity change at the top of this layer comprises a small first-order discontinuity underlain by a 2 km thick transition zone, instead of just a large first-order discontinuity, then both the receiver function data and the WRR data presented here can be satisfied. Finally, the *S*-wave velocities and Poisson's ratios which have been derived in this study are typical of continental crust and do not require extensional processes to explain them.

Key words: anisotropy, crustal structure, Dead Sea, Middle East, *S* waves, transform faults, 2-D modelling.

INTRODUCTION

As part of the DEad SEa Rift Transect (DESERT) project, a seismic wide-angle reflection/refraction profile was carried out in February 2000. The 260 km long, northwest–southeast trending profile extended from Palestine in the northwest, through Israel to Jordan in the southeast (Fig. 1). It crossed the Dead Sea Transform (DST) in the Araba valley about 70 km south of the southern end of the Dead Sea. From an analysis of the compressional (*P*) wave data, a 2-D *P*-wave crustal model beneath the profile has been derived (Weber *et al.* 2004). The purpose of this study is to present a 2-D shear (S) wave model from an analysis of the *S*-wave data. Having information about both the *P*- and *S*-wave crustal velocities provides much better constraints on the gravity and petrological models,

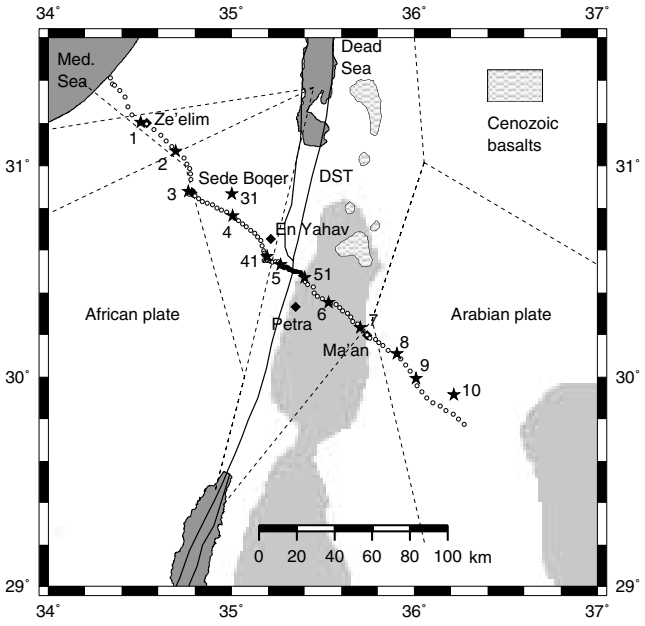

Figure 1. Location map for the 260 km long DESERT wide-angle reflection/refraction (WRR) profile crossing the Dead Sea Transform (DST). During the WRR experiment, 13 shots (stars with numbers) were executed and recorded by 99 three-component instruments (open circles) spaced 1–4.5 km apart along the whole length of the profile and 125 vertical geophone groups (black dots between shots 5 and 51) with 100 m spacing along a 12.5 km long section of the profile in the Araba valley. Previous profiles east (El-Isa *et al.* 1987a,b) and west (Ginzburg *et al.* 1979a,b; Makris *et al.* 1983) of the DST are also shown as dashed lines. Main strands of the DST and Cenozoic volcanics after Garfunkel (1997). Ground above 1000 m is shaded light grey while areas of water are shaded dark grey.

which have been derived by El-Kelani *et al.* (2003) and Förster *et al.* (2004) respectively, in the region of the profile.

The DESERT 2000 wide-angle reflection/refraction experiment comprised on the source side two large quarry blasts of 8500 kg (shot 10 in Fig. 1) and 12 000 kg (shot 31 in Fig. 1), five large borehole shots of 720–950 kg (shots 1, 3, 5, 7 and 9 in Fig. 1) and six small borehole shots of 30–80 kg (shots 2, 4, 41, 51, 6 and 8 in Fig. 1). Whereas the purpose of the large shots and the quarry blasts was to obtain arrivals from the whole crust including the Moho reflection and, if possible, the first arrival refraction through the uppermost mantle, the purpose of the small shots between the large shots was to obtain extra information on the structure of the top of the seismic basement and the overlying cover rocks. The 13 shots were recorded by 99 three-component instruments spaced 1–4.5 km apart along the whole length of the profile and 125 vertical-component geophone groups spaced 100 m apart along a 12.5 km section of the profile between shots 5 and 51 in the Araba valley (Fig. 1). For the 99 three-component instruments, the closest station spacing of 1 km was achieved in the Araba valley where high ambient noise levels were expected. On the shoulders adjacent to the Araba valley where the reflection from the crust–mantle boundary (Moho) was expected to be well recorded at around the critical distance, the station spacing was about 2.5 km. Further out, at the ends of the profile, the station spacing was 4–4.5 km. As the sources were quarry blasts and borehole shots on land and as three-component recordings were made along the whole profile, good quality *S*-wave data were recorded in addition to the *P*-wave data. From the distribution of observation distances (Fig. 2), it can be seen that all the large borehole shots and the two quarry blasts recorded the *S*-wave reflection from the Moho.

Previous crustal-scale wide-angle reflection/refraction profiles in the region include those in Israel in 1977 (Ginzburg *et al.* 1979a,b), the onshore–offshore profile between the northwest end of the DESERT profile and Cyprus in 1978 (Makris *et al.* 1983; Ben-Avraham *et al.* 2002) and those in Jordan in 1984 (El-Isa

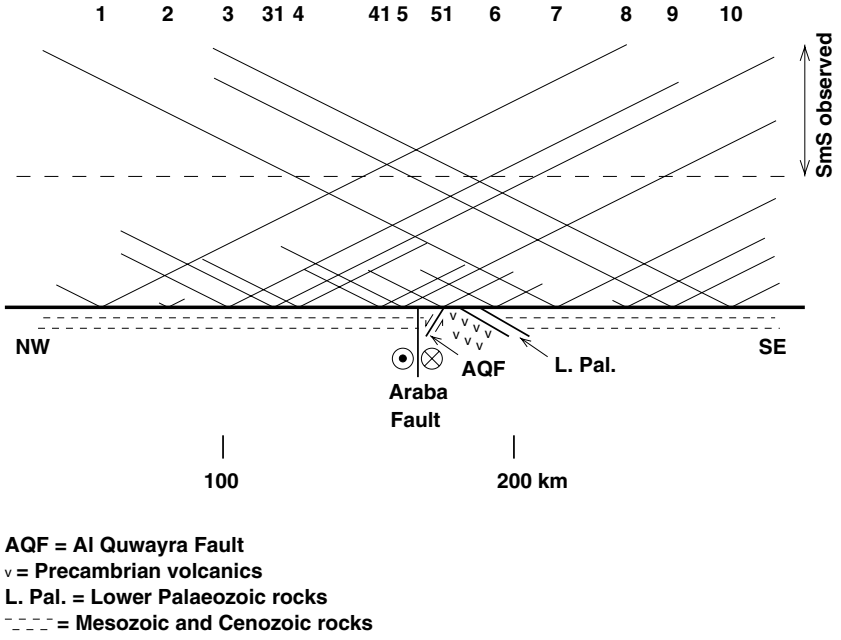

Figure 2. Observation distances of *S* waves from each shot point as marked by the diagonal lines and simplified geological cross-section along the DESERT profile. Shot numbers are marked at the top of the figure. The dashed line marks the average distance of 90 km beyond which the Moho reflection, *SmS*, is observed in addition to the refraction through the upper crust, *Sg*.

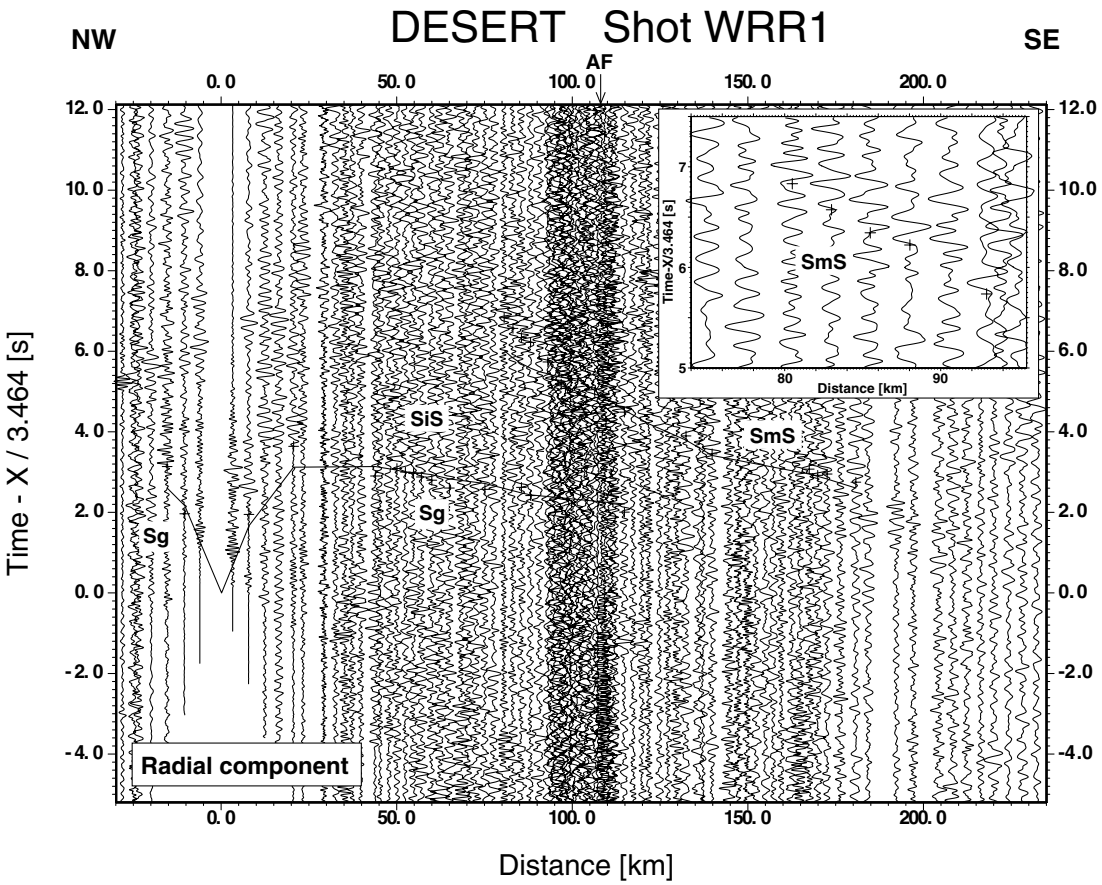

Figure 3. Seismic data from shot 1 recorded along the DESERT wide-angle reflection/refraction (WRR) profile. The record section reduced with a velocity of 3.46 km s^{-1} shows the horizontal radial component of *S*-wave motion in which each trace is normalized individually and bandpass filtered from 2–10 Hz. Lines represent phases calculated from the model in Fig. 10(a), while crosses represent observed traveltime picks. Although there are no observed arrivals for the intracrustal reflection *SiS*, the theoretical position of this phase is shown (dashed line). The inset shows an enlargement of some of the observed *SmS* arrivals between 74 and 95 km distance. Key: *Sg*, refraction through the upper crust; *SiS*, reflection from the top of the lower crust; *SmS*, reflection from the Moho; AF, Araba Fault.

et al. 1987a,b). The majority of these profiles trended approximately north–south and none of them crossed the DST. Those in Israel, including the north–south profile along the Jordan–Dead Sea–Araba valley associated with the DST, used sea shots as the main source of energy, whereas those in Jordan used quarry blasts as the main source of energy. As a result, whereas it was possible to derive a crustal-scale *S*-wave model for Jordan (El-Isa *et al.* 1987b), no crustal-scale *S*-wave model was derived from the 1977 and 1978 profiles for the region west of the DST. Thus the DESERT profile provides for the first time information on the crustal-scale *S*-wave velocity structure from controlled source data for the region west of the DST in Israel and Palestine.

The DST cuts through the northwestern flank of the Nubo-Arabian Shield and, with a total of about 105 km multistage left-lateral shear since about 18 Ma, accommodates the movement between the Arabian Plate and the African Plate (Fig. 1) (Quennell 1958; Freund *et al.* 1970; Garfunkel 1981, 1997). Along most of the DESERT profile rocks of Mesozoic or younger age are exposed at the surface (Fig. 2). Only on the eastern shoulder of the Araba valley, between profile km 176 and 187, does the profile cross outcrops of older rocks. Between profile km 176 and 181 the profile crosses exposures of Precambrian volcanic rocks and between profile km 181 and 187 it crosses outcrops of Lower Palaeozoic rocks. The Araba Fault, the main strand of the DST in this region, is crossed at about profile km 167. Just north of the DESERT profile small outcrops of Cenozoic basalts occur (Fig. 1). A more detailed geological cross-section and map of the central 100 km of the profile are shown in Weber *et al.* (2004).

DATA AND PHASE CORRELATIONS

The data which have been used to derive the *S*-wave velocity structure beneath the DESERT profile are the *S*-wave phases observed on the horizontal components of the three-component instruments. The horizontal components of the geophones were oriented north–south and east–west during the field experiment and first plots of the data, in the form of bandpass filtered (2–10 Hz) distance versus reduced-time record sections, were made of these components. Subsequently, the data were rotated so that record section plots of the radial and transverse components could be made. For each of the five large shots and the two quarry blasts, record sections of either the radial and/or the transverse component are shown (Figs 3–9). In these record sections the *S*-wave reflection from the Moho, *SmS*, can be seen. In the record sections from the small shots which are not shown here, only the refracted arrival through the upper crust, *Sg*, can be recognized (Table 1). From the record sections of the radial and transverse components from all the shots a 2-D *S*-wave velocity model has been derived below the profile (Fig. 10a) and it is

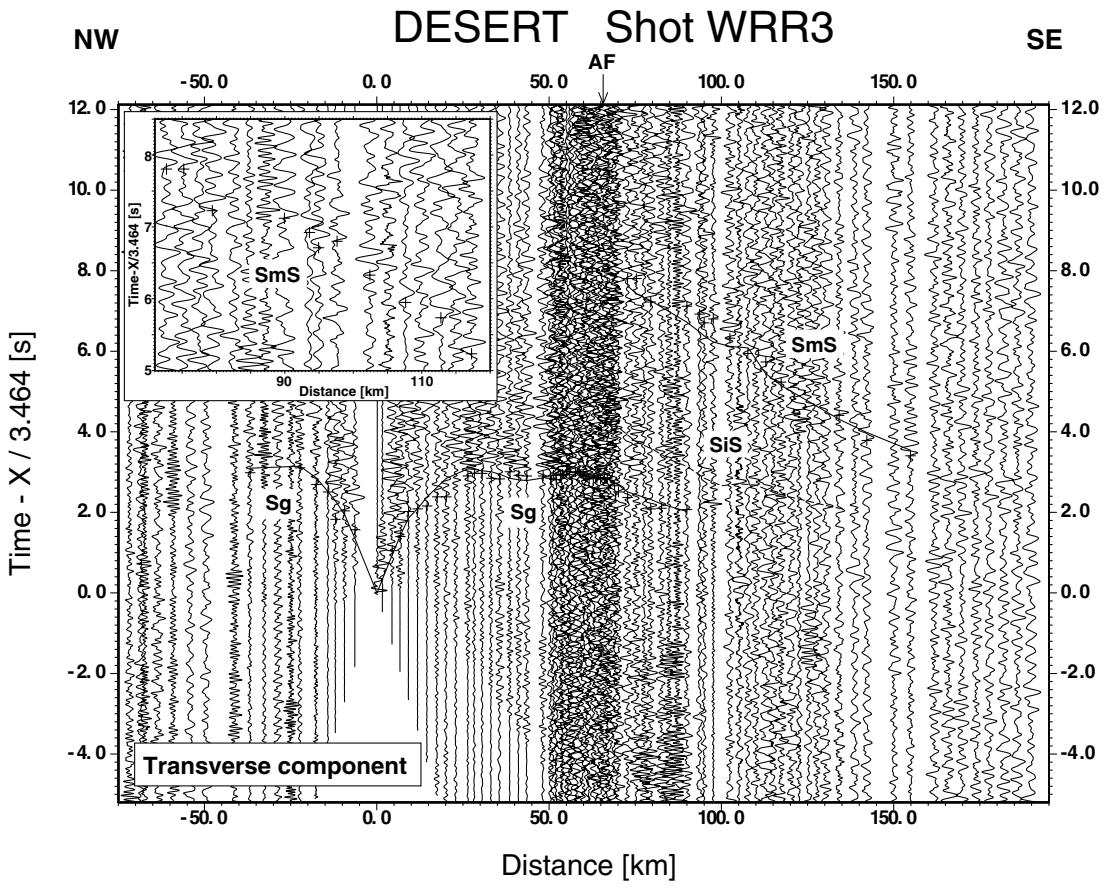

Figure 4. Seismic data from shot 3 recorded along the DESERT wide-angle reflection/refraction (WRR) profile. The record section shows the horizontal transverse component of *S*-wave motion. The data are processed and presented as in Fig. 3. The inset shows an enlargement of some of the observed *SmS* arrivals between 71 and 120 km distance. Key: see Fig. 3.

the theoretical traveltime curves from this model which are plotted together with the observed traveltime picks in the record sections.

In the publication by Weber *et al.* (2004) the *P*-wave record sections are displayed with a reduction velocity of 6 km s^{-1}. If Poisson's ratio is assumed to be 0.25, then the ratio of *P*- to *S*-wave velocity, $V_p/V_s = 1.73$. Thus, in this study, the *S*-wave record sections are shown with a reduction velocity of 3.46 km s^{-1} (6/1.73). Similarly, the timescale on the reduced-time axis of the *S*-wave record sections is plotted with a compression factor of 1.73 with respect to the timescale on the reduced-time axis of the *P*-wave record sections shown by Weber *et al.* (2004). This enables one to directly overlay the *P*- and *S*-wave record sections on each other and qualitatively identify deviations of Poisson's ratio from 0.25 in the crustal structure.

Two major phases have been correlated on the record sections. The first of these is *Sg*, the refracted arrival through the upper crust. Out to distances of 10–30 km the phase has average apparent velocities between 1.5 and 3.0 km s^{-1} while beyond these distances the phase has average apparent velocities of 3.5–3.7 km s^{-1}. From the shots west of the Araba valley, the *Sg* phase can be best recognized on the record sections from the large quarry blast (Fig. 5). On these sections it can be observed at most stations out to the southeastern end of the profile at around 175 km distance, except for the distance range between 55 and 75 km. To the northwest it can also be observed at most stations out to about 55 km distance, beyond which ambient noise conditions at the northwestern end of the profile become too high. Of the two large borehole shots west of the Araba valley, the *Sg* phase can be better observed on the record section from shot 3 (Fig. 4). Here it can be observed at most stations out to about 100 km to the southeast and about 40 km to the northwest. On the section from shot 1 (Fig. 3), it can only be seen well between 40 and 70 km southeast of the shot. From the large shot within the Araba valley (Fig. 6) the *Sg* phase can be recognized at most stations out to about 50 km distance northwest of the shot and 100 km distance southeast of the shot. From the large shots 7 and 9 (Figs 7 and 8) and the quarry blast (Fig. 9) east of the Araba valley, the *Sg* phase can be recognized out to the southeastern end of the profile on the record sections from all three shots. To the northwest it can be best observed on the quarry blast record section, in which it can be observed at most stations out to about 180 km distance, except for distances between 105 and 125 km. On the record section from shot 9, the *Sg* phase can be observed sporadically out to about 140 km to the northwest, whereas on the section from shot 7 it can be seen at most stations between 15 and 105 km to the northwest.

The other major phase which can be recognized on all the record sections from the five large borehole shots and the two quarry blasts is *SmS*, the *S*-wave reflection from the Moho. The phase is observable over the distance range between 70 and 185 km. Often it is recognizable mainly by an increase in energy which is, however, accompanied by a certain coherence between traces over the observable distance range. The record sections in which the highest signal to noise ratio for this phase occurs are those from the large quarry blast west of the Araba valley (Fig. 5) and the large borehole shot within the Araba valley (Fig. 6). In these sections the phase is

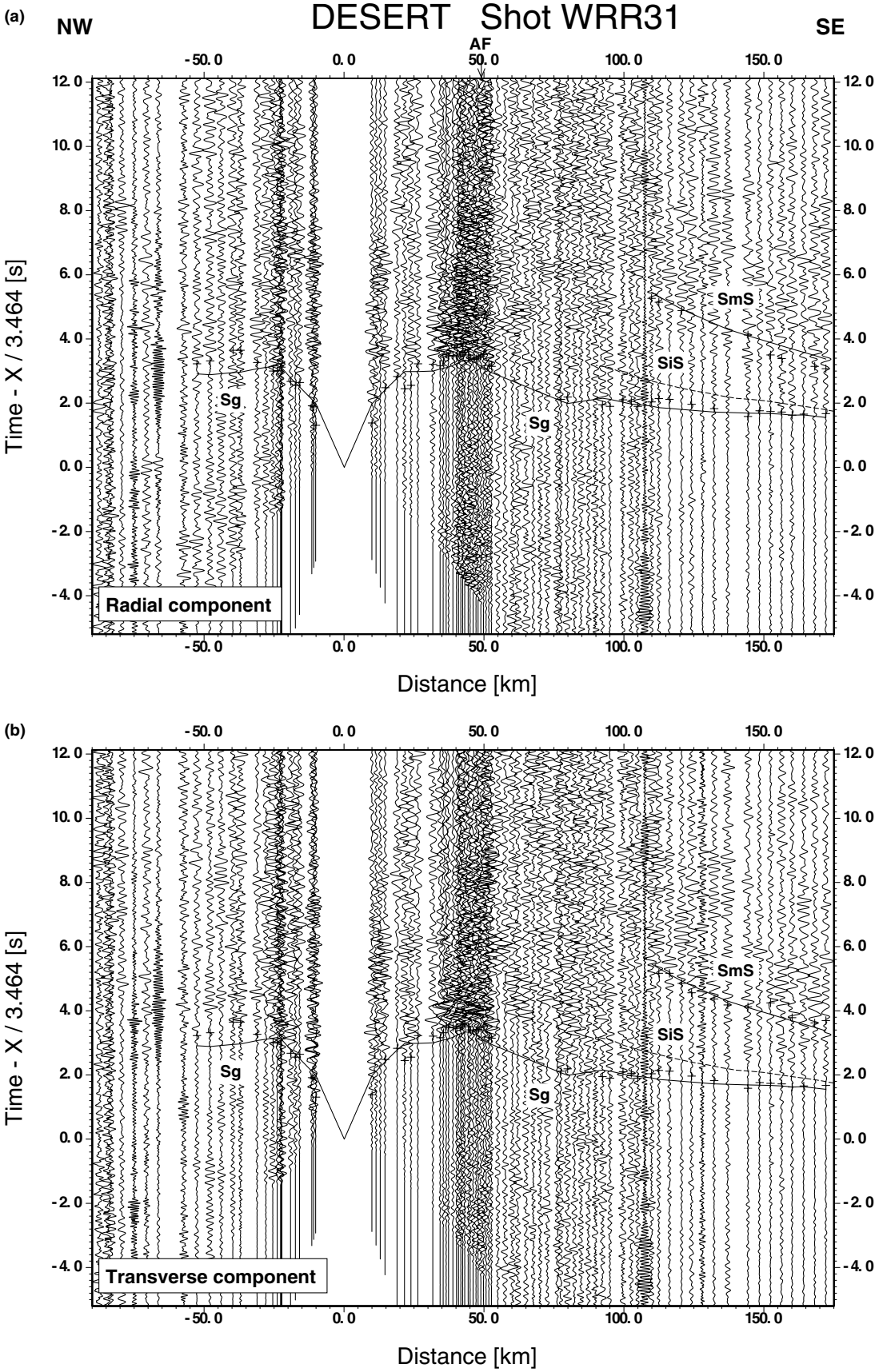

Figure 5. Seismic data from shot 31 (Oron quarry blast) recorded along the DESERT wide-angle reflection/refraction (WRR) profile. The record sections show both the horizontal (a) radial and (b) transverse components of *S*-wave motion. The data are processed and presented as in Fig. 3. Key: see Fig. 3.

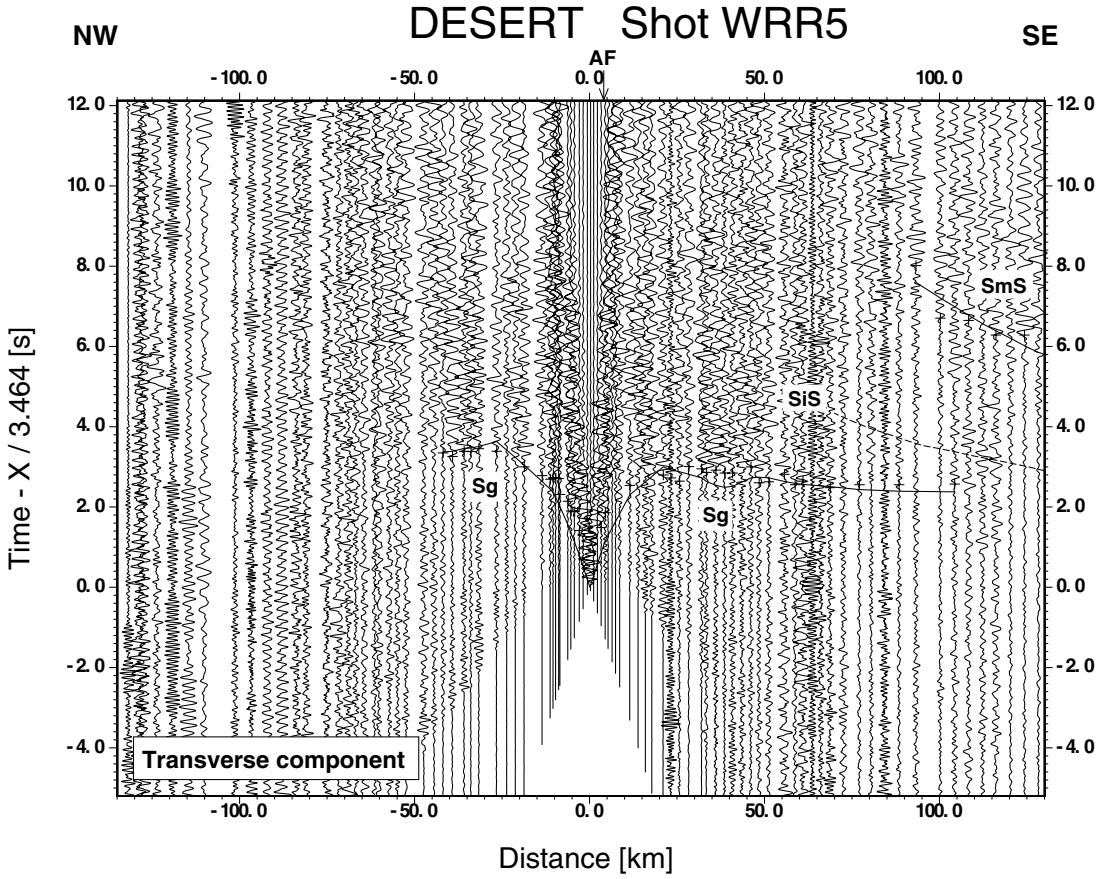

Figure 6. Seismic data from shot 5 recorded along the DESERT wide-angle reflection/refraction (WRR) profile. The record section shows the horizontal transverse component of *S*-wave motion. The data are processed and presented as in Fig. 3. Key: see Fig. 3.

observed from about 100 km southeast of the shot out to the southeastern end of the profile. Further west of the Araba valley, where the crust is somewhat thinner (Weber *et al.* 2004), the record sections from the two large borehole shots, 1 and 3 (Figs 3 and 4), show the *SmS* phase, observed towards the southeast, starting at shorter distances of 70–80 km. In order to show the phase more clearly in regions where denser spacing of seismograms makes it less easy to see the phase on individual traces, enlargements of some of the traces for both shots are shown in insets (Figs 3 and 4). In the enlargement for shot 1 (Fig. 3) quite a good degree of coherence is exhibited by the picked arrivals, whereas in the enlargement for shot 3 (Fig. 4) a fair degree of scattering of the picked arrivals can be seen. East of the Araba valley, on the record sections from the two large borehole shots, 7 and 9 (Figs 7 and 8), the *SmS* phase can be seen towards the northwest from about 100 km out to 160–180 km distance. Further east, where the crust is thicker (Weber *et al.* 2004), the *SmS* phase can be observed to start at a larger distance of around 120 km to the northwest on the record section from the quarry blast near the southeastern end of the profile (Fig. 9). In the enlargements for shots 7, 9 and 10 (Figs 7–9) quite good degrees of coherence are again exhibited by the picked arrivals, especially in the case of shot 10 (Fig. 9) as, despite the relatively low signal-to-noise ratio in the sections, there is still quite a marked increase in energy associated with the *SmS* arrivals.

No intracrustal reflections have been recognized on the *S*-wave record sections. This is in contrast to the *P*-wave record sections, in which a reflection, *PiP* from the boundary between the upper and lower crust could be recognized and in which there were also indications for a possible second intracrustal reflection, *Pi2P* from within the lower crust (Weber *et al.* 2004).

MODELLING

The procedure for the 2-D traveltime modelling of the *S*-wave data was similar to that used by Weber *et al.* (2004) for the *P*-wave data. Using a top-to-bottom approach, in the first step the traveltime data from the *Sg* phase were inverted and in the second step the traveltime data for the *SmS* phase were inverted. The forward problem to determine the rays and traveltimes was solved by classical ray tracing techniques (Červený *et al.* 1977) for the reflected phases, and finite-difference ray tracing based on the eikonal equation (Vidale 1988; Podvin & Lecomte 1991; Schneider *et al.* 1992) for the refracted phases. In the *S*-wave data modelling, the interfaces from the 2-D *P*-wave model (Fig. 10b, Weber *et al.* 2004) were held fixed. Thus, for the inverse problem it was only necessary to determine partial derivatives of the calculated traveltimes with respect to the velocity nodes as described by Lutter *et al.* (1990) and Zelt & Smith (1992). A damped least-squares inversion (see, for example, Zelt & Smith 1992) was then carried out to obtain updates for the velocity nodes, and the forward and inverse problems were repeated until an acceptable convergence between the observed and theoretical traveltimes was reached. In total 457 traveltimes were used for the inversion (Table 1). The model (Fig. 10a) contains six independent velocity parameters (Tables 2 and 3). Although the velocities in the top three layers were generally specified at 5–25 km intervals along the profile, a smaller number of independent velocity parameters

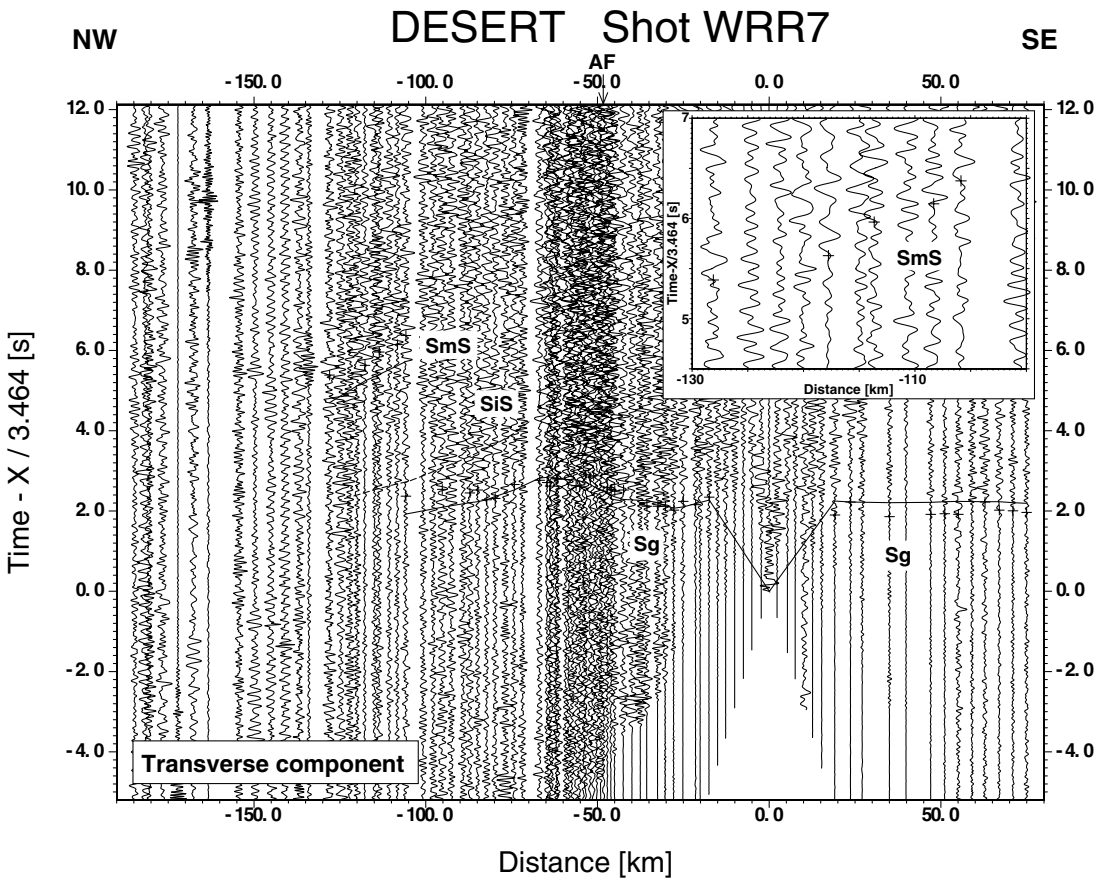

Figure 7. Seismic data from shot 7 recorded along the DESERT wide-angle reflection/refraction (WRR) profile. The record section shows the horizontal transverse component of *S*-wave motion. The data are processed and presented as in Fig. 3. The inset shows an enlargement of some of the observed *SmS* arrivals between −130 and −100 km distance. Key: see Fig. 3.

was solved for in the inversion by grouping the individual nodes together (Table 2). As a result of the inversion, the resolution and standard errors for the various velocity parameters can be calculated (Table 2). These standard error estimates should be viewed as lower bounds of the true errors (Zelt & Smith 1992), especially in the case of the lower crust which probably has an uncertainty in the average *S*-wave velocity of ± 0.2 km s^{-1}. Further, it should be noted that with respect to the accuracy of the Poisson's ratios, if V_p and V_s are accurate to ± 0.1 km s^{-1} then Poisson's ratios are accurate to ± 0.03. ± 0.03 is almost the range of variation within the model presented here (Fig. 10c). However, the fact that the branch of the *Sg* phase with average apparent velocities of 3.5–3.7 km s^{-1} and the *SmS* phase arrive significantly later in the record sections than would be expected if Poisson's ratio were 0.25 everywhere gives confidence that the top two layers and the lower crust do indeed have Poisson's ratios greater than 0.25.

Step 1: Upper crustal *S*-wave velocity structure

Three hundred and sixty-eight traveltime readings from the *Sg* phase were used to determine the *S*-wave velocity structure of the top three layers constituting the upper crust beneath the DESERT profile. Of these, 54 per cent came from the radial component and 46 per cent from the transverse component (Table 1). In the case where there was a reading from both the radial and transverse components, the earlier of the two readings was used in the inversion. In the starting model for the inversion a V_p/V_s of 1.73 was utilized in all three layers. The top layer was modelled with just one independent velocity parameter, while the second and third top layers were both modelled with two independent velocity parameters (Table 2). During the inversion process the vertical velocity gradients in each of the layers were held fixed. As the *a priori* uncertainty in the velocities was set rather generously to be 0.5 km s^{-1} the overall damping factor had to be set to a rather high value of 500 in order to obtain a stable solution (Table 3). After five iterations the average absolute traveltime residual between the theoretical and observed onsets had reduced from 0.41 s ($\chi^2 = 1.86$) in the starting model to 0.30 s ($\chi^2 = 0.99$), with no further significant improvement occurring (Table 3). The normalized traveltime error, χ^2, of 0.99 obtained for the final upper crustal model indicates that the observed data are optimally fitted (Zelt & Smith 1992). This is also indicated by the fact that the average absolute traveltime difference of 0.30 s for the final model is the same as the standard deviation of the traveltime readings (Table 3). However, not all nodes are equally well resolved (Table 2). In particular, the velocity node in the second top layer east of the Araba Fault (AF) is poorly resolved. The reason for this can be seen in the ray diagram (Fig. 11a), which shows that only a few rays actually have their bottoming points in this layer east of the AF.

The fact that the branch of the *Sg* phase with average apparent velocities of 3.5–3.7 km s^{-1} arrives later on the record sections than would be expected if the top two layers had Poisson's ratios of 0.25 indicates that the average structure above the seismic basement (third top layer) has Poissons's ratios greater than 0.25. The results of the inversion confirm this and show that the top layer has average

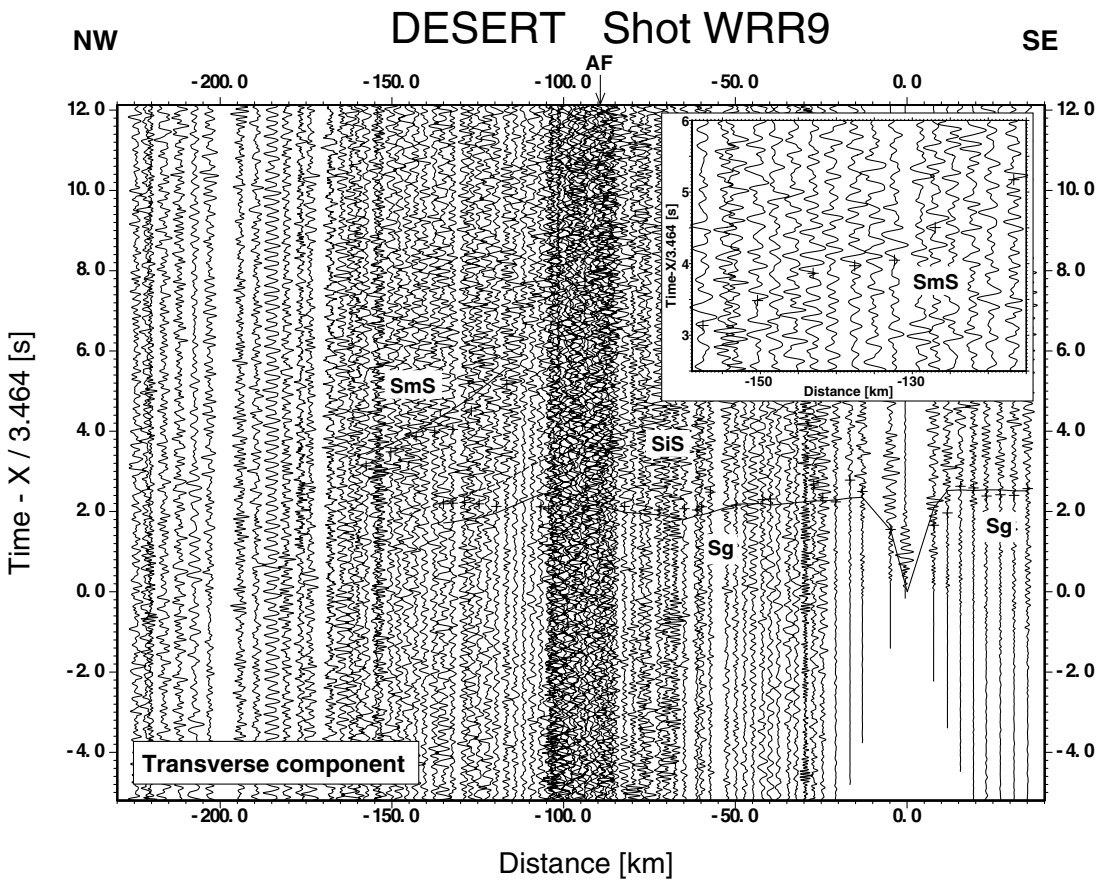

Figure 8. Seismic data from shot 9 recorded along the DESERT wide-angle reflection/refraction (WRR) profile. The record section shows the horizontal transverse component of *S*-wave motion. The data are processed and presented as in Fig. 3. The inset shows an enlargement of some of the observed *SmS* arrivals between −159 and −115 km distance. Key: see Fig. 3.

Poisson's ratios of 0.25–0.26 ($V_p/V_s = 1.73$–1.76) while the second top layer has average Poisson's ratios of 0.29–0.31 ($V_p/V_s = 1.84$–1.91) (Fig. 10c). The fact that the branch of the *Sg* phase with average apparent velocities of 3.5–3.7 km s^{-1}, although late, runs more or less parallel to the branch of the *Pg* phase with average apparent velocities of 6.0–6.25 km s^{-1} on the record sections indicates that the seismic basement (third top layer) has Poisson's ratios close to 0.25 ($V_p/V_s = 1.73$). This is confirmed by the results of the inversion which show *S*-wave velocities of 3.55–3.6 km s^{-1} at the top of the third layer and 3.65–3.75 km s^{-1} at the base of the upper crust, and that the seismic basement has Poisson's ratios of 0.24–0.25 ($V_p/V_s = 1.71$–1.73).

Step 2: Lower crustal *S*-wave velocity structure

Eighty-nine traveltime readings from the *SmS* phase were utilized to invert for the average *S*-wave velocity of the lower crust beneath the DESERT profile. Of these, 47 per cent were from the radial component while 53 per cent were from the transverse component (Table 1). In the starting model for the inversion a V_p/V_s of 1.73 was used for the lower crustal layer. Only one velocity parameter was solved for, and thus although the *a priori* uncertainty in the velocity was set to quite a large value of 0.5 km s^{-1}, the overall damping factor could still be set to just 1 for a stable solution (Table 3). Only one iteration, in which the absolute traveltime residual between the theoretical and observed onsets reduced from 0.75 s ($\chi^2 = 3.53$) to 0.32 s ($\chi^2 = 0.65$), was necessary in order to achieve a solution. The ray diagram (Fig. 11b) indicates that the ray coverage in the lower crust is fairly even and good. The inversion indicates that the average *S*-wave velocity of the lower crust below the DESERT profile is well resolved (Table 2), and the χ^2 value of 0.65 for the final model indicates that the data are adequately fitted by the model.

As many of the *SmS* arrivals have been picked in the face of low signal-to-noise ratios and show a fair degree of scattering as, for example, in the case of shot 3 (Fig. 4), another inversion was performed with only the best data from shots 5 and 31, which showed the best signal-to-noise ratio for this phase, and shot 10 for which a good degree of coherence was shown by the picked arrivals. In this case 38 traveltime readings were used, together with a V_p/V_s of 1.73 for the lower crustal layer in the starting model. Again, only one velocity parameter was solved for and only one iteration, in which the absolute traveltime residual between the theoretical and observed onsets reduced from 0.70 s ($\chi^2 = 3.19$) to 0.23 s ($\chi^2 = 0.33$), was necessary in order to achieve a solution. The inversion indicates that the average *S*-wave velocity of the lower crust is again well resolved (Table 2), and the χ^2 value of 0.33 for the final model again indicates that the data are adequately fitted by the model.

The fact that the *SmS* phase observed on the record sections is up to about 0.8 s later than expected if the seismic basement and the lower crust had Poisson's ratios of 0.25, indicates that the lower crust has Poisson's ratios greater than 0.25, bearing in mind that the seismic basement has been found to have Poisson's ratios of

Table 1. Number of traveltimes picked for each phase (radial component, top row; transverse component, bottom row) from each shot.

Phase	Shot													Total
	1	2	3	31	4	41	5	51	6	7	8	9	10	
Sg	9	1	24	34	7	15	21	13	11	24	1	17	20	197
	6	1	22	24	18	7	18	8	4	14	7	13	29	171
SmS	13		0	7			5			2		3	12	42
	7		14	6			3			5		7	5	47

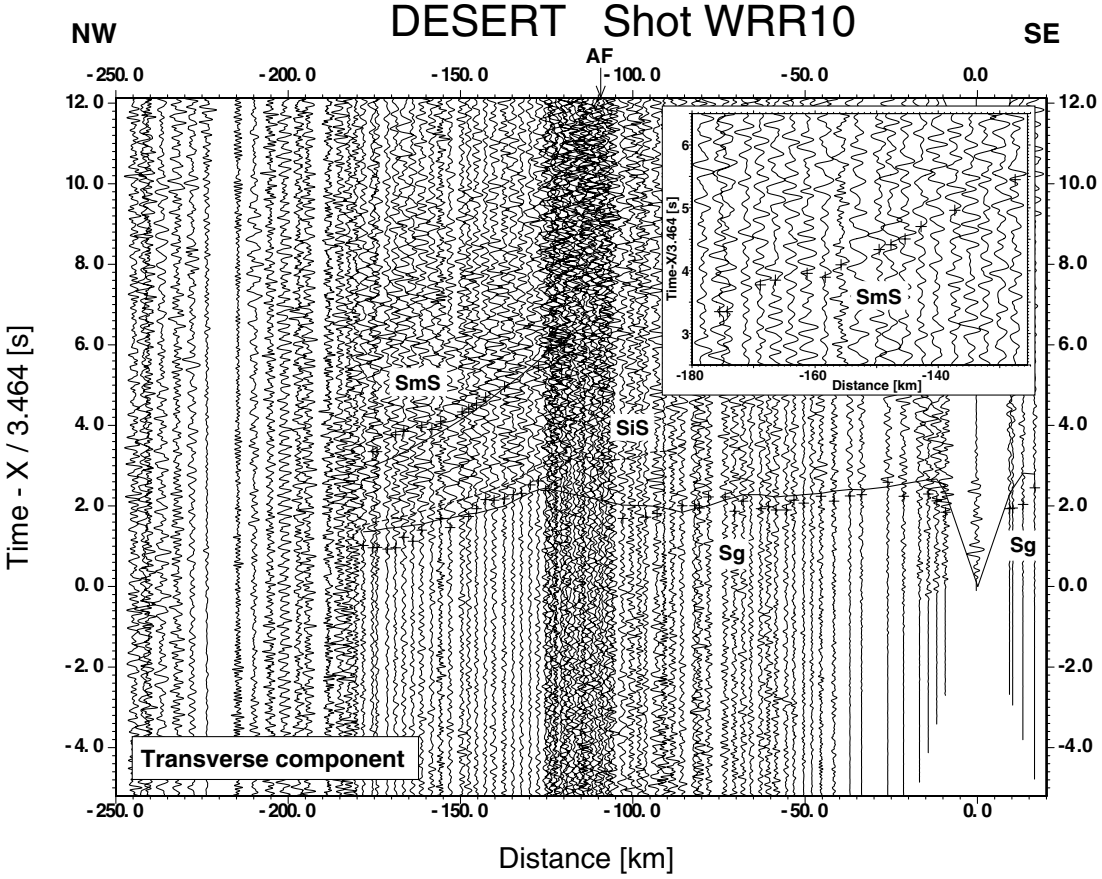

Figure 9. Seismic data from shot 10 (Eshidiyah quarry blast) recorded along the DESERT wide-angle reflection/refraction (WRR) profile. The record section shows the horizontal transverse component of *S*-wave motion. The data are processed and presented as in Fig. 3. The inset shows an enlargement of some of the observed *SmS* arrivals between −180 and −125 km distance. Key: see Fig. 3.

0.24–0.25 ($V_p/V_s = 1.71$–1.73). This is confirmed by the results of both of the inversions described above, which show that the lower crust below the DESERT profile has an average *S*-wave velocity of around 3.75 km s^{-1} and an average Poisson's ratio of about 0.27 ($V_p/V_s = 1.78$) (Figs 10a and c). As a result, the contrast in *S*-wave velocities across the boundary between the upper and lower crust is minimal, being no greater than 0.1 km s^{-1}, and thus it is not surprising that the intracrustal reflected phase *SiS*, corresponding to *PiP*, from the boundary between the upper and lower crust, was not observed on the record sections. Average crustal *S*-wave velocities beneath the DESERT profile range from 3.3–3.5 km s^{-1} and whole crustal Poisson's ratios from 0.26–0.27 ($V_p/V_s = 1.76$–1.78). West of the DST in Israel and Palestine the average *S*-wave velocity of about 3.7 km s^{-1} for the seismic basement is almost as high as that of the lower crust, whereas to the east of the DST under the Jordanian highlands the average *S*-wave velocity of 3.6 km s^{-1} for the seismic basement is 0.1–0.2 km s^{-1} smaller than that of the lower crust. As the refracted *S*-wave phase, *Sn*, through the uppermost mantle was not observed in this experiment and also not in previous controlled source experiments in the region, there is no information on the *S*-wave velocity of the uppermost mantle.

DISCUSSION AND SUMMARY

From the observation of a lower crustal multiple (LCM) in a receiver function study, Mohsen *et al.* (2005) found evidence for a basal crustal layer with a high *S*-wave velocity east of the DST (Fig. 12). Introducing a basal crustal layer with a high *S*-wave velocity of 4.0 km s^{-1} into a 1-D average of the model shown here and calculating synthetic seismograms produces a wide-angle intracrustal reflected phase which is more or less as prominent as the *SmS* phase beyond about 120 km distance where it arrives about 1 s earlier than

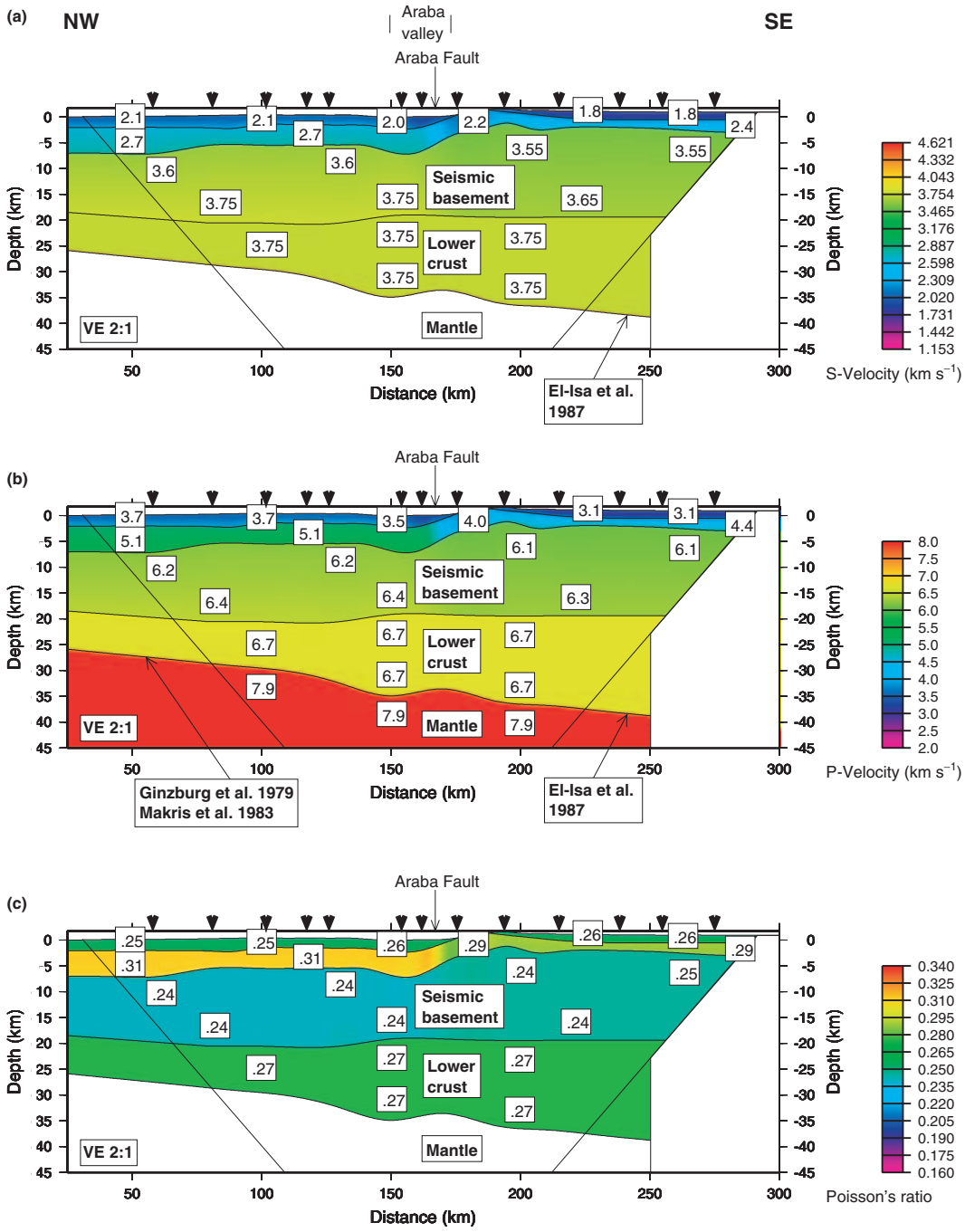

Figure 10. (a) *S*-wave velocity model derived by inverting the observed traveltime picks shown in Figs 3–9 . (b) *P*-wave velocity model (after Weber *et al.* 2004). (c) Poisson's ratio model derived from (a) and (b) for the DESERT profile. Velocities, correct to the nearest 0.05 km s^{-1} for the seismic basement and the lower crust in the *S*-wave model, are in km s^{-1}. Triangles at the top of each section represent the shot points. Only the region within the diagonal lines is resolved in this study. To the northwest the boundaries and *P*-wave velocities are based on previous work by Ginzburg *et al.* (1979a,b) and Makris *et al.* (1983) while to the southeast the boundaries and *P*- and *S*-wave velocities are based on El-Isa *et al.* (1987a,b).

the *SmS* phase (Fig. 13a). Thus it could be expected that this phase would have been seen in the observed wide-angle data. A way out of this problem is to design a model with a combination of a smaller discontinuity and a strong gradient at the top of the basal crustal layer with a high *S*-wave velocity. For example, a model with an *S*-wave velocity jump from 3.7 to 3.85 km s^{-1} at the discontinuity and an increase in *S*-wave velocity from 3.85 to 4.0 km s^{-1} through the top 2 km of the basal crustal layer, only produces a wide-angle phase which is more or less as prominent as the *SmS* phase beyond about 140 km distance where it only arrives 0.4–0.5 s earlier than the *SmS* phase and thus may be practically indistinguishable from the *SmS* phase (Fig. 13b). However, a model with a velocity jump from 3.7 to 3.85 km s^{-1} at the discontinuity and an increase in velocity from 3.85 to 4.0 km s^{-1} through the top 2 km of the basal crustal layer, produces essentially the same lower crustal multiple for waves with a dominant period of 3 s as does a model with a

Table 2. Some input parameters for the inversion and the resolution (R) and standard errors after Zelt & Smith (1992) for the various nodes for the final iteration.

Parameter type	No of nodes	R	Std. error (km s^{-1})	Node coordinates (km)
Top layer velocity	1	0.96	0.09	0, 20, 40, 60, 70, 80, 90, 100, 110, 120, 130, 140, 150, 155, 160, 165, 170, 175, 190, 200, 210, 220, 240, 260, 280, 300
2nd layer velocity	2	0.55 0.38	0.33 0.39	0, 20, 40, 60, 80, 90, 100, 110, 120, 130, 140, 150, 160, 165 170, 180, 190, 200, 210, 220, 230, 240, 250, 260, 270, 280, 300
3rd layer velocity	2	0.78 0.93	0.23 0.13	0, 20, 40, 60, 80, 100, 120, 140, 160 175, 195, 215, 235, 255, 275, 300
Lower crust velocity, *SmS* all	1	0.9997	0.01	0, 300
Lower crust velocity, *SmS* best	1	0.9995	0.01	0, 300

Table 3. Some input parameters and results of the inversion. χ^2 is the normalized traveltime error, σ_d is the standard deviation of the traveltime readings, σ_m is the *a priori* uncertainty in the model parameters and D is the overall damping factor (see, e.g. Zelt & Smith 1992). In the middle column, all *SmS* arrivals were included in the inversion, while in the right column only the best *SmS* arrivals from shots 5, 10 and 31 were included in the inversion.

Parameter	Phase		
	Sg	*SmS* all	*SmS* best
Ave. δt start model (s)	0.41	0.75	0.70
Ave. δt final model (s)	0.30	0.32	0.23
χ^2 start model	1.86	3.53	3.19
χ^2 final model	0.99	0.65	0.33
σ_d (s)	0.3	0.4	0.4
σ_m velocity (km s^{-1})	0.5	0.5	0.5
D	500.0	1.0	1.0

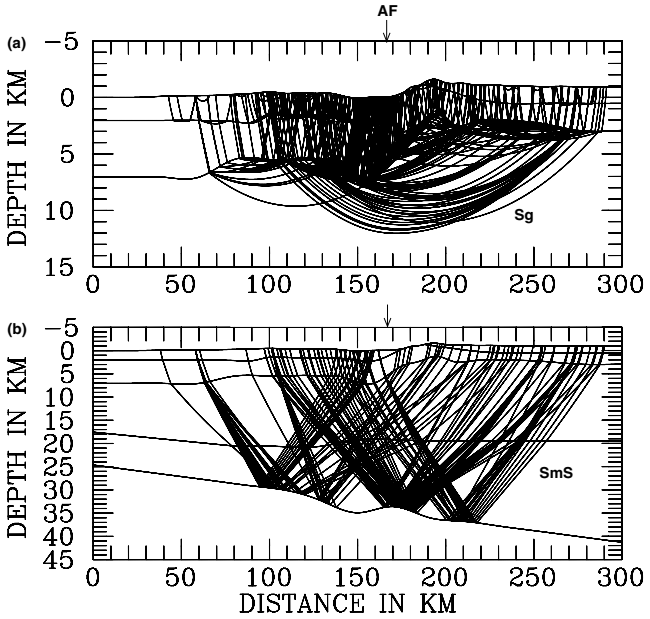

Figure 11. Ray diagrams for the final iterations of (a) the *Sg* phase and (b) the *SmS* phase. AF, Araba Fault.

discontinuity from 3.7 to 4.0 km s^{-1}. In order to illustrate this, receiver functions (Fig. 12) were computed using the reflectivity method (Müller 1985) for a single slowness, i.e. for an incident plane wave. The gradients in the models (Fig. 13) are approximated by a stack of homogeneous layers with the individual layer thicknesses being significantly less than the dominant signal period. The traces were rotated from vertical and radial to L and Q containing only the P and SV wavefields respectively, as in Mohsen *et al.* (2005). The traces were also convolved with a Gauss function with a parameter of 1.3 s^{-1} (Owens *et al.* 1984), to make them compatible with the 3 s dominant period of the data of Mohsen *et al.* (2005). Thus if the structure at the top of the basal crustal layer with a high S-wave velocity is more complicated than just a simple discontinuity then one could expect to observe the lower crustal multiple from the top of this layer in low-frequency receiver function data but would not necessarily expect to observe the intracrustal reflection in the wide-angle S-wave data. To emphasize what occurs in the case of a model with no high S-wave velocity, basal crustal layer, note the absence of the *Si2S* phase in the synthetic wide-angle data (Fig. 13c) and the LCM in the synthetic receiver functions (Fig. 12). In a shear wave splitting analysis using teleseismic *SKS* data, Rümpker *et al.* (2003) found evidence for anisotropy in both the crust and uppermost mantle beneath the DESERT profile.

For the crust the best fitting model of Rümpker *et al.* (2003) consisted of three lateral blocks varying from 20 to 40 km in width with directions for the horizontal symmetry axis ranging from N7°W to N21°W and magnitudes for the anisotropy ranging from 5.1 per cent to 7.2 per cent. The DESERT profile trends N45°W which is about 30° off the horizontal symmetry axis if N15°W is taken as the average for the three blocks. Taking the average magnitude of the anisotropy for the three blocks to be 6 per cent and calculating phase velocity surfaces for a transverse isotropic medium with a horizontal symmetry axis, it can be observed that at 30° off the symmetry axis the difference in the two shear wave velocities is less than 0.01 km s^{-1} and thus very small (Fig. 14). In the observed wide-angle S-wave data there are no consistent signs for anisotropy. Particle motion plots for observed arrivals from the *Sg* and *SmS* phases show no consistent pattern of one S-wave arriving before the other. Particle motion plots and synthetic seismograms along a profile at 30° off the symmetry axis of a 35 km thick transverse isotropic medium with a horizontal symmetry axis and 6 per cent anisotropy (Fig. 14) are shown for the *Sg* and *SmS* phases at distances of 150 and 160 km respectively (Fig. 15). These are about the maximum distances out to which these phases are observed. The particle motion plots show signals which are not linearly polarized and which thus may be

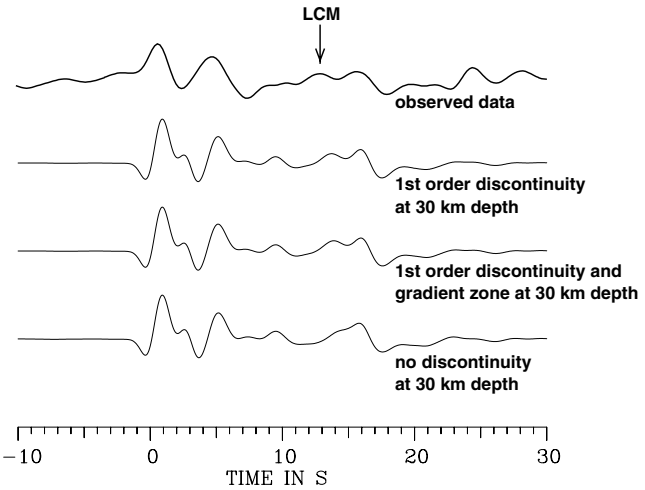

Figure 12. An observed receiver function from Mohsen *et al.* (2005) from the east side of the DST (top), shown together with receiver functions calculated for the velocity models shown in Fig. 13(a) (upper middle), Fig. 13(b) (lower middle) and Fig. 13(c) (bottom). LCM marks the position of the lower crustal multiple observed by Mohsen *et al.* (2005). The LCM is prominent in both the observed data and the top two synthetic receiver functions and it is more or less identical in the two receiver functions derived from velocity models with a discontinuity and, in one case, a gradient zone at 30 km depth. However, it is absent in the bottom receiver function derived from a velocity model with no discontinuity at 30 km depth.

thought to show indications for the presence of anisotropy. However, in the case of the *Sg* phase the traveltime difference between the fast *S*-wave which is dominant on the transverse component and the slow *S*-wave which is dominant on the radial component at 150 km distance is only about 0.1 s. This is smaller than the standard deviation of the traveltime picks of the *Sg* phase. In the case of the *SmS* phase the picture is further complicated by the fact that there are not just two split *S*-waves but three, when the converted reflections between the fast and slow *S* waves are taken into account. At 160 km distance the traveltime difference between the fast *S*-wave which is dominant on the transverse component and the converted reflections which are dominant on the radial component is about 0.24 s. This is again smaller than the standard deviation of the traveltime picks of the *SmS* phase. Thus it is probably not surprising that there are no consistent signs of anisotropy in the observed data. Thus the model of Rümpker *et al.* (2003) is compatible with the wide-angle *S*-wave observations made along the DESERT profile. In order to have had a realistic chance to detect shear wave splitting, the wide-angle *S*-wave observations would have to have been made along a profile oriented at about N75°E.

As stated above, the present results provide for the first time information from controlled source data on the *S*-wave velocity structure of the crust west of the DST in Israel and Palestine. To the east of the DST, beneath the Jordanian highlands, a comparison between the present results and those of the experiment in 1984 (El-Isa *et al.* 1987b) reveals many similarities. The results of the experiment in 1984 showed that the top two layers have Poisson's ratios of about 0.25 ($V_p/V_s = 1.73$) except in northwest Jordan where they exhibit a Poisson's ratio of around 0.32 ($V_p/V_s = 1.94$), the seismic basement has a Poisson's ratio of about 0.25 ($V_p/V_s = 1.73$), the lower crust has Poisson's ratios of 0.29–0.32 ($V_p/V_s = 1.84$–1.94) and the contrast in *S*-wave velocities between the upper and lower crust is small. An intracrustal reflected phase from the boundary between the upper and lower crust was also not observed on the *S*-wave record sections from the experiment in 1984. In the present study the top two layers have average *S*-wave velocities ranging from 1.8–2.7 km s^{-1} and average Poisson's ratios greater than 0.25. The seismic basement has average *S*-wave velocities of around 3.6 km s^{-1} east of the DST and about 3.7 km s^{-1} west of the DST and Poisson's ratios of 0.24–0.25 ($V_p/V_s = 1.71$–1.73), while the lower crust has an average *S*-wave velocity of about 3.75 km s^{-1} and an average Poisson's ratio of about 0.27 ($V_p/V_s = 1.78$). Thus the similarities between the two studies are quite apparent, although the Poisson's ratios in the lower crust in the present study are not quite as high as those from the experiment in 1984.

From an analysis of the near-vertical incidence reflection data and the wide-angle reflection/refraction *P*-wave data from the DESERT project, Weber *et al.* (2004) concluded that fault perpendicular extension does not play an important role in the dynamics of the DST. This statement is supported by the present analysis of the wide-angle reflection/refraction *S*-wave data from the DESERT project. The *S*-wave velocities and Poisson's ratios which have been derived in this study are typical of continental crust and do not require extensional processes to explain them. The *S*-wave velocities and Poisson's ratios derived in this study for the seismic basement can be explained by felsic compositions typical of continental upper crust while those for the lower crust can be explained by mafic compositions typical of continental lower crust. East of the DST, the *S*-wave velocities and Poisson's ratios derived in this study for the seismic basement are similar to those derived by El-Isa *et al.* (1987b) in southwest Jordan where the seismic profile crossed exposed seismic basement consisting of Precambrian rocks mainly of granitic and granodioritic compositions. The tendency for the *P*- and *S*-wave velocities of the seismic basement to be somewhat higher west of the DST may indicate a change to a somewhat less felsic composition west of the DST. The change from felsic to mafic compositions at the boundary between the upper and lower crust at about 20 km depth, in conjunction with the moderate heat flow of 50–60 mW m^{-2} in the region (Eckstein & Simmons 1978; Förster *et al.* 2004), probably explains the occurrence of earthquakes at lower crustal depths in the vicinity of the DST (Aldersons *et al.* 2003). This is because the lower-strength, quartz-dominated lower part of the upper crust in which earthquakes might not occur is replaced by the higher-strength, mafic lower crust in which earthquakes can occur (see e.g. Smith & Bruhn 1984). A more detailed compositional stratification of the crust in the vicinity of the DESERT profile is provided by Förster *et al.* (2004).

From the present analysis of the wide-angle reflection/refraction *S*-wave data from the DESERT project, no evidence was found for igneous intrusions in the crust associated with the nearby outcrops of Cenozoic basalts (Fig. 1). In contrast, strong reflections in the near-vertical incidence reflection data east of the DST and intermittent reflections in the wide-angle *P*-wave data mainly east of the DST from about 30 km depth could be from mafic intrusions associated with the nearby Cenozoic volcanism (Weber *et al.* 2004). The nearby Cenozoic volcanism could, however, be the northernmost extension of such volcanism associated with the opening of the Red Sea (Altherr *et al.* 1990) rather than with any fault perpendicular extension associated with the DST. The slight change in the *P*- and *S*-wave velocities of the seismic basement across the DST (Fig. 10), the existence of strong reflections in the near-vertical incidence reflection data in the lower crust only to the east of the DST (Weber *et al.* 2004) and the likely existence of a basal crustal layer with a high *S*-wave velocity only to the east of the DST (Mohsen *et al.* 2005) can best be explained by the 105 km left-lateral movement along the transform.

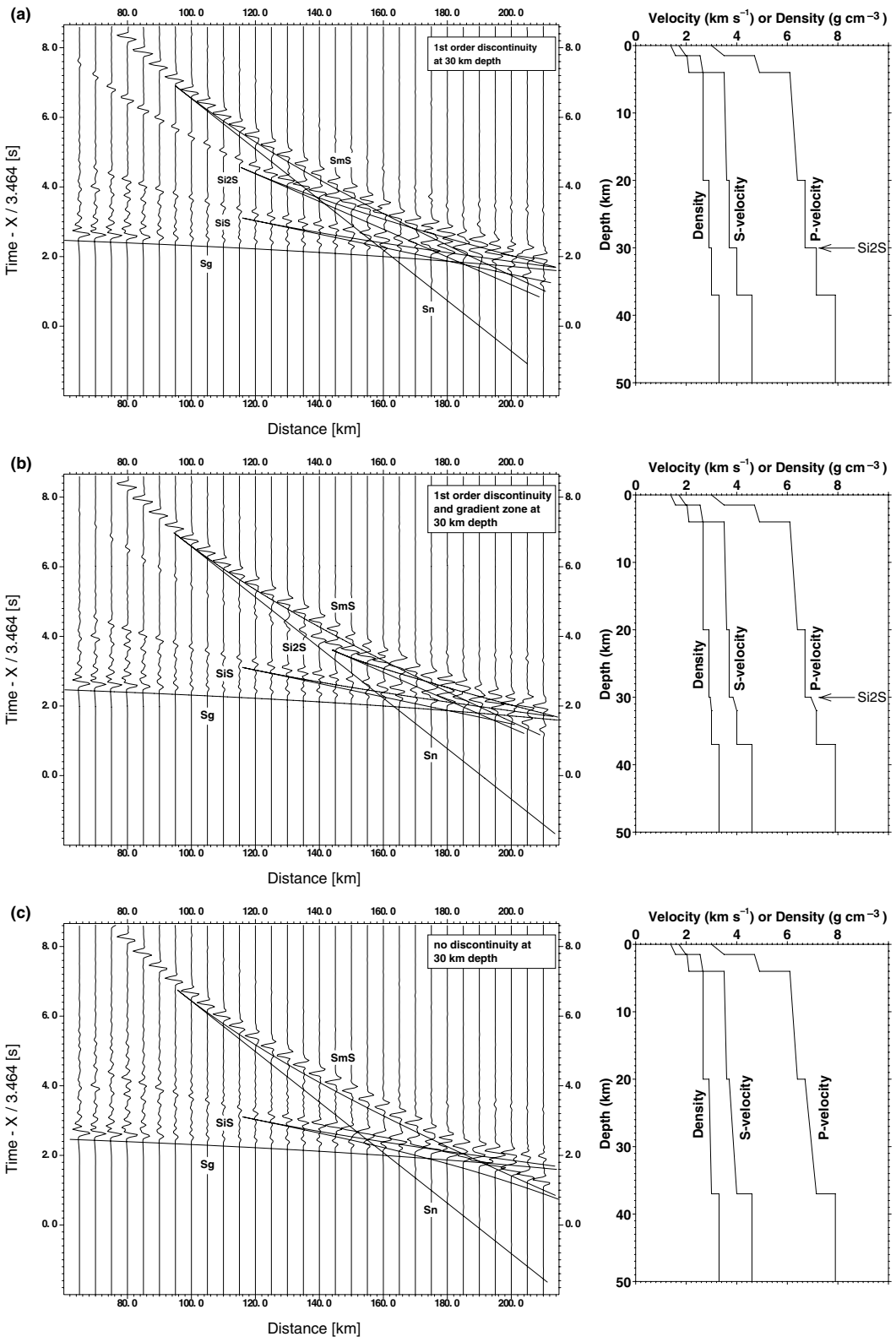

Figure 13. (a) *S*-wave synthetic seismogram section calculated using the reflectivity method (Fuchs & Müller 1971) for a model with a homogeneous, high *S*-wave velocity, basal crustal layer. The record section reduced with a velocity of 3.46 km s^{-1} shows the transverse component of *S*-wave motion in which each trace is normalized individually. Continuous lines represent phases calculated from the velocity model on the right. Density (ρ) is dependent on *P*-wave velocity (V_p) according to the relationship $\rho = 0.3788V_p + 0.252$ (Birch 1961). Key: see Fig. 3; additionally *Si2S* is the reflection which is prominent beyond 120 km distance, from the top of the high *S*-wave velocity, basal crustal layer. (b) *S*-wave reflectivity seismograms for a model with a gradient at the top of the high *S*-wave velocity, basal crustal layer. Note that phase *Si2S* does not become prominent until 140 km distance. The data are processed and presented as in (a). (c) *S*-wave reflectivity seismograms for a model with no high *S*-wave velocity, basal crustal layer. Note that phase *Si2S* is absent in this case. The data are processed and presented as in (a).

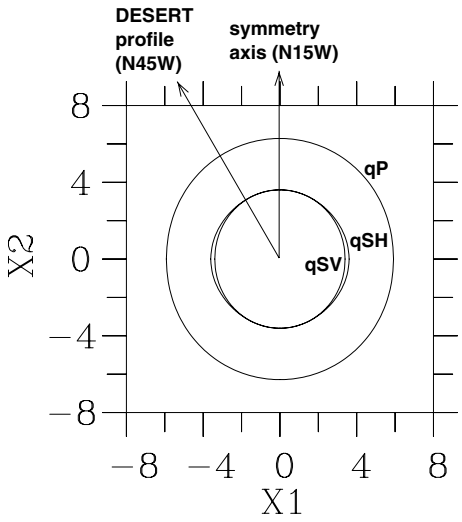

Figure 14. Horizontal section at X3 = 0 through the phase velocity surfaces of *qP*, *qSH* and *qSV* for a transverse isotropic medium with a horizontal symmetry axis in the X2 direction and 6 per cent anisotropy. Velocities are in km s^{-1}.

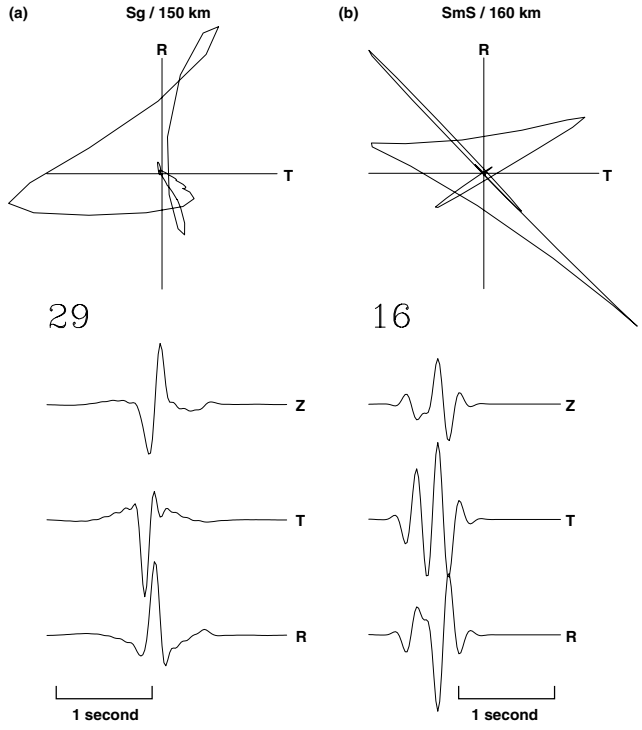

Figure 15. Theoretical seismograms and particle motion plots for (a) the *Sg* phase at 150 km distance and (b) the *SmS* phase at 160 km distance. The seismograms have been calculated along a profile at 30° off the symmetry axis of a 35 km thick transverse isotropic medium with a horizontal symmetry axis and 6 per cent anisotropy. In (a) the seismograms have been calculated using the reflectivity method (Booth & Crampin 1983; Nolte 1988) whereas in (b) the seismograms have been calculated using ray theory (Červený 1972; Červený *et al.* 1977; Gajewski & Pšenčík 1987). Key: Z, vertical component; R, radial component; T, transverse component.

ACKNOWLEDGMENTS

The DESERT project was funded by the Deutsche Forschungsgemeinschaft, the GeoForschungsZentrum (GFZ) Potsdam and the Minerva Dead Sea Research Centre. The National Ministry of Infrastructure of Israel, the Natural Resources Authority of Jordan and the An-Najah National University in Nablus, Palestine are thanked for their support. Our contractors, the Geophysical Institute of Israel, the Site Group (Jordan) and the Chemical and Mining Industries (Jordan), are thanked for their excellent work under difficult logistic conditions. The cooperation of the Oron mine (Israel) and the Eshidiyah mine (Jordan) is also gratefully acknowledged. The instruments were provided by the Geophysical Instrument Pool of the GFZ Potsdam. Discussions with A. Förster and H.-J. Förster have also helped to improve the manuscript.

REFERENCES

Aldersons, F., Ben-Avraham, Z., Hofstetter, A., Kissling, E. & Al-Yazjeen, T., 2003. Lower-crustal strength under the Dead Sea basin from local earthquake data and rheological modeling, *Earth planet. Sci. Lett.,* **214,** 129–142.

Altherr, R., Henjes-Kunst, F. & Baumann, A., 1990. Asthenosphere versus lithosphere as possible sources for basaltic magmas erupted during formation of the Red Sea: constraints from Sr, Pb and Nd isotopes, *Earth planet. Sci. Lett.,* **96,** 269–286.

Ben-Avraham, Z., Ginzburg, A., Makris, J. & Eppelbaum, L., 2002. Crustal structure of the Levant Basin, eastern Mediterranean, *Tectonophysics,* **346,** 23–43.

Birch, F., 1961. The velocity of compressional waves in rocks to 10 kilobars, part 2, *J. geophys. Res.,* **66,** 2199–2224.

Booth, D.C. & Crampin, S., 1983. The anisotropic reflectivity technique: theory, *Geophys. J. R. astr. Soc.,* **72,** 755–766.

Červený, V., 1972. Seismic rays and ray intensities in inhomogeneous anisotropic media, *Geophys. J. R. astr. Soc.,* **29,** 1–13.

Červený, V., Molotkov, I.A. & Pšenčík, I., 1977. *Ray Method in Seismology,* University of Karlova, Prague.

Eckstein, Y. & Simmons, G., 1978. Measurements and interpretation of terrestrial heat flow in Israel, *Geothermics,* **6,** 117–142.

El-Isa, Z., Mechie, J., Prodehl, C., Makris, J. & Rihm, R., 1987a. A crustal structure study of Jordan derived from seismic refraction data, *Tectonophysics,* **138,** 235–253.

El-Isa, Z., Mechie, J. & Prodehl, C., 1987b. Shear velocity structure of Jordan from explosion seismic data, *Geophys. J. R. astr. Soc.,* **90,** 265–281.

El-Kelani, R., Goetze, H., Rybakov, M., Hassouneh, M. & Schmidt, S., 2003. Crustal structure along the DESERT 2000 transect inferred from 3-D gravity modelling, *EOS, Trans. Am. geophys. Un.,* **84**(46), Fall Meeting Supplement, abstract S21F-0399.

Förster, H.-J., Oberhänsli, R., Sobolev, S.V., Förster, A., Stromeyer, D. & DESERT Group, 2004. Lithosphere composition and thermal regime across the Dead Sea Transform in Israel and Jordan, *EOS, Trans. Am. geophys. Un.,* **85**(17), Joint Assembly Supplement, abstract T11A-05.

Freund, R., Garfunkel, Z., Zak, I., Goldberg, M., Weissbrod, T. & Derin, B., 1970. The shear along the Dead Sea rift. *Phil. Trans. R. Soc. Lond.,*A, **267,** 107–130.

Fuchs, K. & Müller, G., 1971. Computation of synthetic seismograms with the reflectivity method and comparison with observations, *Geophys. J. R. astr. Soc.,* **23,** 417–433.

Gajewski, D & Pšenčík, I., 1987. Computation of high-frequency seismic wavefields in 3-D laterally inhomogeneous anisotropic media, *Geophys. J. R. astr. Soc.,* **91,** 383–411.

Garfunkel, Z., 1981. Internal structure of the Dead Sea leaky transform (rift) in relation to plate kinematics, *Tectonophysics,* **80,** 81–108.

Garfunkel, Z., 1997. The history and formation of the Dead Sea basin, in *The Dead Sea—the Lake and its Setting,* Oxford Monographs on Geology and Geophysics No 36, pp. 36–56, eds Niemi, T.M., Ben-Avraham, Z. & Gat, J.R., Oxford University Press, Oxford.

Ginzburg, A., Makris, J., Fuchs, K., Prodehl, C., Kaminski, W. & Amitai, U., 1979a. A seismic study of the crust and upper mantle of the Jordan–Dead Sea Rift and their transition toward the Mediterranean Sea, *J. geophys. Res.,* **84,** 1569–1582.

Ginzburg, A., Makris, J., Fuchs, K., Perathoner, B. & Prodehl, C., 1979b. Detailed structure of the crust and upper mantle along the Jordan–Dead Sea Rift, *J. geophys. Res.,* **84,** 5605–5612.

Lutter, W.J., Nowack, R.L. & Braile, L.W., 1990. Seismic imaging of upper crustal structure using traveltimes from the PASSCAL Ouachita experiment, *J. geophys. Res.,* **95,** 4621–4631.

Makris, J., Ben-Avraham, Z., Behle, A., Ginzburg, A., Giese, P., Steinmetz, L., Whitmarsh, R.B. & Eleftheriou, S., 1983. Seismic refraction profiles between Cyprus and Israel and their interpretation, *Geophys. J. R. astr. Soc.,* **75,** 575–591.

Mohsen, A., Hofstetter, R., Bock, G., Kind, R., Weber, M., Wylegalla, K. & DESERT Group, 2005. A receiver function study across the Dead Sea Transform, *Geophys. J. Int.*, **160,** doi: 10.1111/j.1365.246X.2005.02534.x.

Müller, G., 1985. The reflectivity method: a tutorial, *J. Geophys.,* **58,** 153–174.

Nolte, B., 1988. Erweiterung und Anwendung des Reflektivitätsprogrammes für anisotrope Medien, *Diploma Thesis,* Karlsruhe University.

Owens, T.J., Zandt, G. & Taylor, S.R., 1984. Seismic evidence for an ancient rift beneath the Cumberland plateau, Tennessee: a detailed analysis of broadband P waveforms, *J. geophys. Res.,* **89,** 7783–7795.

Quennell, A.M., 1958. The structural and geomorphic evolution of the Dead Sea rift, *Q. J. geol. Soc. Lond.,* **114,** 2–24.

Podvin, P. & Lecomte, I., 1991. Finite difference computation of traveltimes in very contrasted velocity models: a massively parallel approach and its associated tools, *Geophys. J. Int.,* **105,** 271–284.

Rümpker, G., Ryberg, T., Bock, G. & Desert Seismology Group, 2003. Boundary-layer mantle flow under the Dead Sea transform fault inferred from seismic anisotropy, *Nature,* **425,** 497–501.

Schneider, W.A., Ranzinger, K.A., Balch, A.H. & Kruse, C., 1992. A dynamic programming approach to first arrival traveltime computation in media with arbitrarily distributed velocities, *Geophysics,* **57,** 39–50.

Smith, R.L. & Bruhn, R.L., 1984. Intraplate extensional tectonics of the eastern Basin Range: Inferences on structural style from seismic reflection data, regional tectonics, and thermal-mechanical models of brittle–ductile deformation, *J. geophys. Res.,* **89,** 5733–5762.

Vidale, J., 1988. Finite-difference calculation of travel times, *Bull. seism. Soc. Am.,* **78,** 2062–2076.

Weber, M. *et al.*, 2004. The crustal structure of the Dead Sea Transform, *Geophys. J. Int.,* **156,** 655–681, doi:10.1111/j.1365-246X.2004.02143.x.

Zelt, C.A. & Smith, R.B., 1992. Seismic traveltime inversion for 2-D crustal velocity structure, *Geophys. J. Int.,* **108,** 16–34.